



Received 9 October 2024  
Accepted 16 July 2025

Edited by T. J. Sato, Tohoku University, Japan

**Keywords:** absorption correction; diffraction; neutron scattering; X-ray scattering.

# Neutron absorption correction and mean path length calculations for multiple samples with arbitrary shapes: application to highly absorbing samples on the Multi-Axis Crystal Spectrometer at NIST

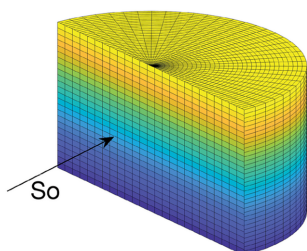
Jose A. Rodriguez-Rivera<sup>a,b\*</sup> and Chris Stock<sup>c</sup>

<sup>a</sup>Department of Materials Science, University of Maryland, College Park, MD 20742, USA, <sup>b</sup>NIST Center for Neutron Research, National Institute of Standards and Technology, 100 Bureau Drive, Gaithersburg, MD 20899, USA, and <sup>c</sup>School of Physics and Astronomy, University of Edinburgh, Edinburgh EH9 3JZ, United Kingdom. \*Correspondence e-mail: jose.rodriguez@nist.gov

Recent advancements in cold neutron instrumentation, designed to achieve the energy resolution necessary for studying strongly correlated materials, have driven the need for sophisticated modeling of neutron spectroscopy data from highly neutron-absorbing materials. These absorption effects are often highly dependent on both angular orientation and wavelength. To address this, the finite-volume algorithm for absorption correction developed by Wuensch & Prewitt [Z. Kristallogr. (1965), **122**, 24–59] is examined in this paper in the context of cold neutron spectroscopy. This algorithm is based on the numerical integration of the transmission function, where three-dimensional quadratic surfaces define the sample boundaries. The algorithm can also determine the mean path length required for second-extinction calculations. We apply this method to neutron inelastic scattering measurements of an irregularly shaped CeRhIn<sub>5</sub> single crystal using the Multi-Axis Crystal Spectrometer at NIST. The algorithm has been expanded to correct for the absorption of multiple coaligned samples. We show that this procedure can account for the angle-dependent absorption, and the technique can be used to correct the data and plan experiments.

## 1. Introduction

The current developments at high-intensity neutron sources offer a dramatic improvement in the ability to probe the dynamic properties of materials at the nanoscale. The new high-intensity neutron spectrometers allow us to study smaller samples and samples containing atoms with large absorption cross sections. Understanding the angular dependency of absorption corrections in neutron scattering experiments is increasingly important for comprehending the properties of materials. In particular, many strongly correlated electronic systems of interest over the past decade (Stewart, 1984; Pfleiderer, 2009; Dai, 2015) contain highly absorbing elements, which will give a strong angular dependence to the magnetic cross section and are not inherent to the system properties of interest. Examples from our own work conducted at the NIST Center for Neutron Research and at the ISIS Muon and Neutron Source (Rutherford Appleton Laboratory, Didcot, UK) include materials containing elements such as iridium (Na<sub>2</sub>IrO<sub>3</sub>; Choi *et al.*, 2012) (bond directional exchange in iridates), indium [CeCoIn<sub>5</sub> (Stock *et al.*, 2008; Stock *et al.*, 2012b) and CeRhIn<sub>5</sub> (Stock *et al.*, 2015; Brener *et al.*, 2024)] (unconventional superconductivity) and rhodium [CeRhSi<sub>3</sub>



(Pásztorová *et al.*, 2019) and  $\text{YbRh}_2\text{Si}_2$  (Stock *et al.*, 2012a)] (heavy fermion quantum criticality). The absorption cross sections of these elements are plotted as a function of neutron energy in Fig. 1. Many of these systems have been studied recently because developments in cold neutron instrumentation have allowed improved resolution in characterizing the magnetic dynamics of these compounds. Although Fig. 1 illustrates that the absorption decreases with increasing energy, the physical properties of interest in many of these materials require fine energy resolution and hence the low energy transfers provided by cold neutrons where the absorption cross section increases dramatically.

The absorption corrections for such materials are significant because the data are notably affected by a combination of neutron transmission (attenuation) and sample geometry, leading to misleading interpretations. Several techniques have been developed to calculate absorption corrections quickly and accurately. The transmission factors calculated by Rouse *et al.* (1970) are still widely used due to their easy accessibility in crystallographic tables. However, they are limited only to cylindrical and spherical samples. Busing & Levy (1957) developed one of the first numerical methods to calculate the absorption for an arbitrary shape. The de Meulenaer and Tompa method (de Meulenaer & Tompa, 1965; Alcock *et al.*, 1972) divides the sample into Howells polyhedra and applies an analytical formula to calculate the absorption. The advantage of such a method is the short computing time required to calculate the transmission for a single sample and detector position. Still, the sample must be divided into Howells polyhedra for every sample rotation and detector configuration. The Wuensch & Prewitt (1965) finite-volume algorithm is a generalization of the Busing and Levy technique that only requires the sample to be approximated by quadratic plane surfaces. Other absorption correction algorithms have been developed for specific cases (Hermann & Ermrich, 1987; Montesin *et al.*, 1991; Blessing, 1995; Schmitt & Ouladdiaff,

1998; Angel, 2004; Bowden & Ryan, 2010; Dallmann *et al.*, 2024; Lu *et al.*, 2024). The *MANTID* project comprises a collection of absorption correction algorithms, including a calculator for an arbitrary sample defined as a collection of cuboids (Arnold *et al.*, 2014).

The present paper reviews an updated version of the generalized Wuensch and Prewitt algorithm for inelastic neutron scattering data. The algorithm has been extended to calculate the absorption for multiple coaligned samples. The same method can be used to find the mean path length of the beam to calculate the Zachariasen extinction correction (Becker & Coppens, 1974). We demonstrate the method with measurements on an irregularly shaped  $\text{CeRhIn}_5$  single crystal using the Multi-Axis Crystal Spectrometer (MACS) at the NIST Center for High Resolution Neutron Scattering (CHRNS).

## 2. The method

The transmission is defined as  $T = I/I_0$ , where  $I_0$  is the intensity of the incident beam and  $I$  is the intensity of the diffracted beam from a crystal. The neutron transmission coefficient  $T$  can be calculated using the Beer–Bourger–Lambert law (Bourger, 1729; Beer, 1852),

$$\langle T \rangle = \frac{1}{V} \int_V \exp[-(\mu t + \mu_0 t_0)] dV, \quad (1)$$

where  $t$  and  $t_0$  are the path lengths of the scattered and incident beam, respectively,  $\mu$  and  $\mu_0$  are the linear absorption coefficients for the incident and the scattered beam, respectively, and  $dV$  is a given volume element. We replace equation (1) for a discrete sum over all  $(x_p, y_q, z_r)$  volume elements by its discrete equivalent (Wuensch & Prewitt, 1965):

$$\langle T \rangle = \frac{1}{M} \sum_{pqr} \exp[-(\mu t + \mu_0 t_0)]. \quad (2)$$

We can find the mean path length used for the Zachariasen extinction correction, which is defined as  $\bar{T} = (1/T)(\delta T/\delta\mu)$  (Coppens & Hamilton, 1970), where

$$\bar{T} = \frac{1}{M} \frac{\sum_{pqr} (t + t_0) \exp[-\mu(t + t_0)]}{\sum_{pqr} \exp[-\mu(t + t_0)]}. \quad (3)$$

### 2.1. Discretization of the volume

To evaluate equations (2) and (3) numerically, we divide our sample into volume elements. The most common discretization method divides the volume into finite and regular rectangular cuboids (volume elements). The first step is to define a box containing the sample as follows:

$$\begin{aligned} x_{\min} &\leq x \leq x_{\max}, \\ y_{\min} &\leq y \leq y_{\max}, \\ z_{\min} &\leq z \leq z_{\max}. \end{aligned} \quad (4)$$

Then, we subdivide our box into desired intervals  $N_x$ ,  $N_y$  and  $N_z$ . The array of grid points will be defined as a collection of

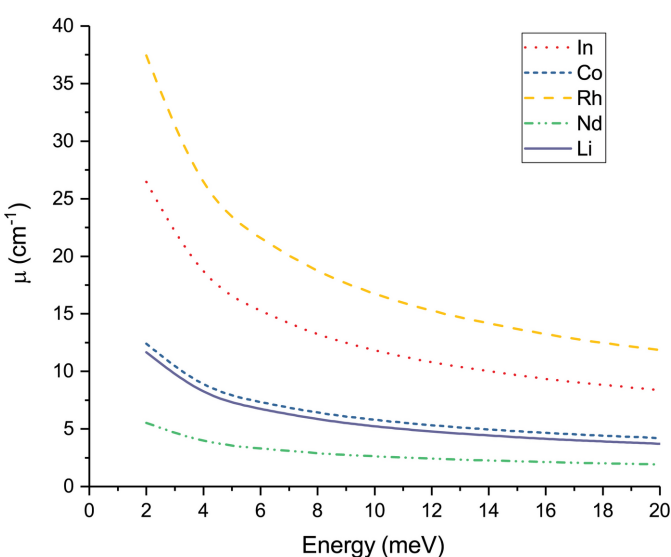


**Figure 1**

Neutron linear attenuation factors for different elements as a function of energy (Sears, 1992).

indices  $p$ ,  $q$  and  $r$ . Each  $(x_p, y_q, z_r)$  volume element center position will be given by

$$\begin{aligned} x_p &= x_{\min} - \frac{x_{\max} - x_{\min}}{2N_x} + p \frac{x_{\max} - x_{\min}}{N_x}, \\ y_q &= y_{\min} - \frac{y_{\max} - y_{\min}}{2N_y} + q \frac{y_{\max} - y_{\min}}{N_y}, \\ z_r &= z_{\min} - \frac{z_{\max} - z_{\min}}{2N_z} + r \frac{z_{\max} - z_{\min}}{N_z}. \end{aligned} \quad (5)$$

## 2.2. Finding $t$ and $t_0$

The main challenge in solving equations (2) and (3) is finding the neutron path lengths  $t$  and  $t_0$  for each  $\Delta V$  element. We can simplify our problem by defining our sample as a collection of one or more quadratic surfaces  $f(x, y, z)$ . Each quadratic surface is expressed in the following form (Wuensch & Prewitt, 1965; Cychosz & Waggenspack, 1992):

$$\begin{aligned} f(x, y, z) = Ax^2 + By^2 + Cz^2 + Dxy + Eyz + Gzx + Hx \\ + Iy + Jz = F. \end{aligned} \quad (6)$$

The defined sample must not have re-entrant angles, meaning that any volume element inside the sample must have a direct line of sight to the other volume elements. The transmission for samples with re-entrant angles can be calculated by constructing a collection of smaller samples with no re-entrant angles and applying the algorithm to calculate the transmission for multiple samples, as explained in the following sections.

To find the path lengths  $t$  and  $t_0$  along which the neutron travels inside the sample, we define our scattered and incident neutron beam unit vectors  $\mathbf{s}$  and  $\mathbf{s}_0$ , respectively, as in Fig. 2,

$$\begin{aligned} \mathbf{s} &= s_x \hat{\mathbf{x}} + s_y \hat{\mathbf{y}} + s_z \hat{\mathbf{z}}, \\ \mathbf{s}_0 &= s_{0x} \hat{\mathbf{x}} + s_{0y} \hat{\mathbf{y}} + s_{0z} \hat{\mathbf{z}}. \end{aligned} \quad (7)$$

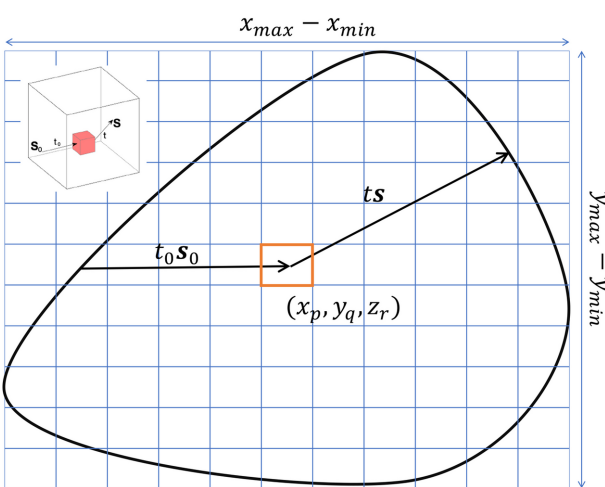


**Figure 2**

Discretizations of volume elements. The sample is divided into  $N_x$ ,  $N_y$  and  $N_z$ . Each square represents a volume element.  $\mathbf{s}_0$  and  $\mathbf{s}$  represent the incident and scattered beam unit vectors, respectively.  $t_0$  and  $t$  represent the incident and scattered beam path lengths inside the sample, respectively.

If a neutron travels a distance  $t_0$  from the sample boundary defined by a quadratic surface to a volume element  $(x_p, y_q, z_r)$  and a distance  $t$  from the same volume element to the respective sample boundary following the path defined by  $\mathbf{s}_0$  and  $\mathbf{s}$ , we have the following (Wuensch & Prewitt, 1965):

$$\begin{aligned} x - x_p &= -t_0 s_{0x}, & x - x_p &= ts_x, \\ y - y_q &= -t_0 s_{0y}, & y - y_q &= ts_y, \\ z - z_r &= -t_0 s_{0z}, & z - z_r &= ts_z. \end{aligned} \quad (8)$$

Note that  $t_0$  is defined as a negative multiple of  $s_0$  to make the positive  $t_0$  the correct distance once we solve equation (9). The substitution of equations (7) and (8) into the bounding function [equation (6)] leads to the general solution for where the incident and scattered beams  $\mathbf{s}_0$  and  $\mathbf{s}$  intersect the quadratic surface (Wuensch & Prewitt, 1965; Cychosz & Waggenspack, 1992):

$$U t_0^2 + V t_0 + W_0 = 0, \quad (9)$$

with

$$U_0 = As_{0x}^2 + Bs_{0y}^2 + C_{0z}^2 + Ds_{0x}s_{0y} + Es_{0y}s_{0z} + Fs_{0z}s_{0x}, \quad (10)$$

$$\begin{aligned} V_0 = & -[2Ax_p s_{0x} + 2By_q s_{0y} + 2Cz_r s_{0z} + D(x_p s_{0y} + y_q s_{0z}) \\ & + E(y_q s_{0z} + z_r s_{0y}) + G(z_r s_{0x} + x_p s_{0z}) + Hs_{0x} \\ & + Is_{0y} + Js_{0z}], \end{aligned} \quad (11)$$

$$\begin{aligned} W_0 = & Ax_p^2 + By_q^2 + Cz_r^2 + Dx_p y_q + Ey_q z_r + Gz_r x_p + Hx_p \\ & + Iy_q + Jz_r - F. \end{aligned} \quad (12)$$

Similarly, for  $t$  we have

$$Ut^2 + Vt + W = 0, \quad (13)$$

where  $U$  and  $W$  are the same as in equations (10) and (12). The sign of  $V$  is now positive, opposite to  $V_0$  as defined in equation (11). Equations (9) and (13) have two solutions for  $t_0$  and  $t$ ,

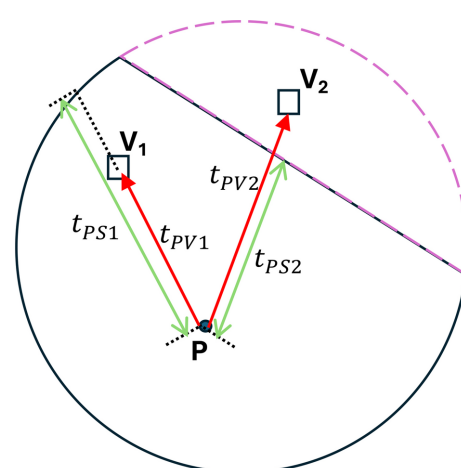


**Figure 3**

Two-dimensional projection of a sphere intersected by a plane. Point  $P$  defines the region of interest. Volume element  $V_1$  lies within this region, as the direct line from  $V_1$  to  $P$  is unobstructed by any bounding quadratic surface. In contrast, the volume element  $V_2$  is outside the region of interest because a bounding surface blocks its path to  $P$  (the plane).

where the positive solution is always the correct one. If the surface given in equation (6) is a plane, the solution is expressed as follows (Busing & Levy, 1957; Wuensch & Prewitt, 1965):

$$t_0 = -W_0/V_0, \quad t = -W/V. \quad (14)$$

A point  $P$  inside the sample must be defined. This point will help determine whether any volume element is localized inside or outside the sample volume when the quadratic surfaces defining the sample contain two or more enclosed volumes, such as a sphere bisected by a plane, as described in Fig. 3. The volume element must satisfy the following conditions to be evaluated in equations (2) and (3): (i)  $t_0$  and  $t$  must have positive values, and (ii) the volume elements must be connected to any other volume element within the sample by a straight line without interference from a quadratic surface. All other volume elements must be ignored. To determine whether the volume element meets the second condition, we compute two distances: the distance from the reference point  $P$  to the volume element,  $t_{PV}$ , and the distance from  $P$  to the first surface encountered along the direction towards the volume element,  $t_{PS}$ , as illustrated in Fig. 3. If a volume element such as  $V1$  is located inside the sample, the direct path from  $P$  to  $V1$  is unobstructed, and thus  $t_{PV1} < t_{PS1}$ . In contrast, for a volume element outside the sample, such as  $V2$ , the path intersects a quadratic surface before reaching the element, resulting in  $t_{PV2} > t_{PS2}$ . A collection of  $n$  quadratic surfaces with the form of equation (6) could result in more than one positive value for  $t_0$  and  $t$ . In that case, we always take the smallest positive values of  $t_0$  and  $t$  that satisfy the second condition.

### 2.3. Sample orientation and kinematic equations

Once the quadratic surfaces have been defined, we set the sample orientation to match the initial scattering conditions. To simplify the calculations, we fix the sample and only rotate the unitary vectors  $s_0$  and  $s$  of the incident and scattered beams. Note that the beam will rotate opposite to the sample. Depending on the diffractometer's geometry and the sample's alignment, the diffraction transformation can be applied (Busing & Levy, 1967; Thorkildsen *et al.*, 1999). For the examples in this paper, we utilize rotation transformations about the  $x$ ,  $y$  and  $z$  axes as necessary.

For a typical triple-axis spectrometer or a time-of-flight neutron spectrometer, where the measured scattering process takes place in the  $xy$  plane, we define  $Q_x$  perpendicular to the incident beam,  $Q_y$  in the direction of the incident beam  $s_0$  and  $\theta_{\text{sample}} = 0^\circ$ . We can apply the kinematic equations to calculate the sample's neutron transmission as a reciprocal-space function. For convenience, we apply the transformation operations to the incident and scattered beams  $s_0$  and  $s$  rather than to the boundary functions. For certain sample positions  $A_3$  (defined as the sample rotation in the scattering plane  $\theta_{\text{sample}}$ ) and  $A_4$  (defined as the detector angle in the scattering plane  $2\theta_{\text{sample}}$ ), we define the kinematic equations as (Squires, 2012; Shirane *et al.*, 2006)

$$|\mathbf{Q}|^2 = \mathbf{k}_i^2 + \mathbf{k}_f^2 - 2|\mathbf{k}_i||\mathbf{k}_f| \cos A_4, \quad (15)$$

$$\omega = (\pm) \arccos \left( \frac{\mathbf{k}_i^2 + \mathbf{Q}^2 - \mathbf{k}_f^2}{2|\mathbf{k}_i||\mathbf{Q}|} \right) + (\pi/2 - A_3), \quad (16)$$

$$\mathbf{Q} = |\mathbf{Q}|(\cos \omega \hat{\mathbf{i}} + \sin \omega \hat{\mathbf{j}}), \quad (17)$$

where  $\mathbf{k}_i$  and  $\mathbf{k}_f$  are the initial and final wavevectors, respectively, and  $\mathbf{Q} = \mathbf{k}_i - \mathbf{k}_f$ . The  $\pm$  factor in equation (16) corresponds to  $\pm A_4$  values.

### 2.4. Simple geometrical examples: spheres, cylinders, half-cylinders

The method has been implemented in MATLAB and Python. The program repositories contain several pre-defined samples, including spheres, cylinders, half-cylinders, prisms and cuboids. This paper will show examples of transmission calculations for a sphere and cylinder as a comparison with the results from *International Tables for Crystallography* (2006) (referred to as the 'IUCr tables') and the transmission calculation in the full range of  $\theta$ - $2\theta$  rotation for a half-cylinder sample. We define the sphere sample with one quadratic surface as in equation (6) with  $A = 1$ ,  $B = 1$ ,  $C = 1$  and  $F = r^2$ . All other values are zero. The linear absorption coefficient value is  $\mu r = 2.5$  (Fig. 4).

The cylinder sample has a radius  $r = 1$  cm and a height  $l = 0.5$  cm. Three boundary functions define the cylinder as in equation (6). The first boundary equation is a circle in the  $xy$  plane with values of  $A = 1$ ,  $B = 1$  and  $F = r^2$ . All other values are zero. Two planes dissect the cylinder and define the height. The first plane  $z = l/4$  is defined with  $J = 1$  and  $F = l/4$ . The other plane,  $z = -l/4$ , is defined by  $J = 1$  and  $F = -l/4$ . The scattering plane lies in the  $xy$  plane. The linear absorption correction is defined as  $\mu r = 2.5$  to compare with the IUCr tables. For both samples, we used a grid of  $N_x = N_y = N_z = 55$ . The calculated transmissions for the sphere and the cylinder completely agree with the results in the IUCr tables.

The half-cylinder is an infinite cylinder with a radius of 1 cm dissected by three planes, one at  $y = 0$  and two at  $z = 0.5$  and

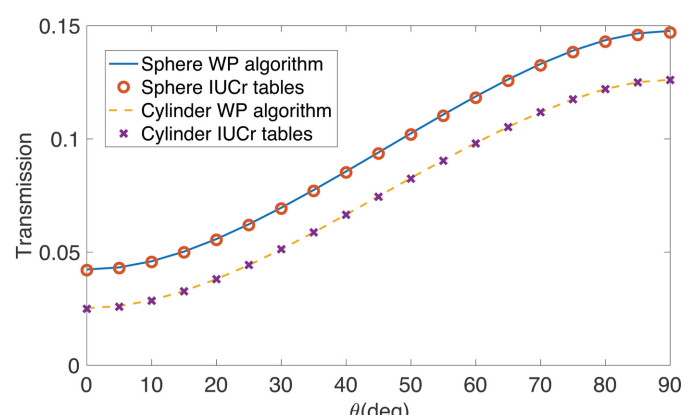
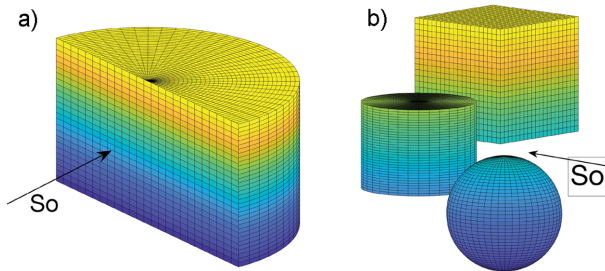
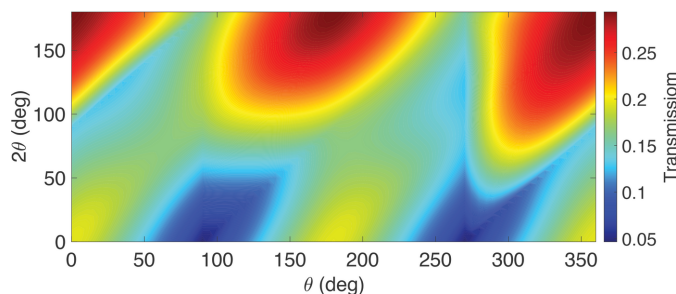


Figure 4

Comparison of the calculated transmission for  $\mu r = 2.5$  of a sphere and a cylinder sample with the IUCr tables.

**Figure 5**

Neutron transmission example figures. (a) The half-cylinder lies in the  $xy$  plane, with its flat surface oriented parallel to the  $x$  axis. (b) Three-sample configuration: the cylinder is oriented vertically along the  $z$  axis. In both configurations, the incident beam vector  $s_0$  points along the  $y$  axis when  $\theta_{\text{sample}} = 2\theta_{\text{sample}} = 0$ .

**Figure 6**

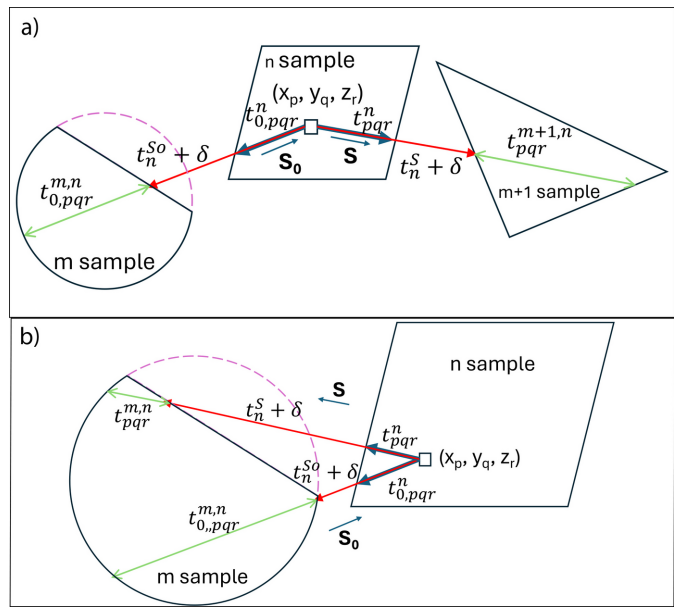
Neutron transmission for a half-cylinder  $r = 0.5$  cm as a function of the sample rotation angle  $\theta$  and the detector position  $2\theta$ . The sample has a linear absorption coefficient factor of  $\mu = 2.0 \text{ cm}^{-1}$ .

$z = -0.5$  as in Fig. 5(a). The linear absorption coefficient  $\mu = 2 \text{ cm}^{-1}$ . Fig. 6 illustrates the relationship between the transmission, the sample rotation angle  $\theta$  and the detector position  $2\theta$ . For this example,  $\theta = 0^\circ$  when the  $y$  axis is parallel to the  $s_0$  incident beam. The sample angle  $\theta$  and the detector position  $2\theta$  rotate in the same direction.

## 2.5. Multiple samples

To calculate the total transmission for  $N$  samples, we define each  $n$ th sample as a collection of quadratic surfaces as in equation (6). Each sample must have a defined point inside to specify the volume of interest. Each  $n$ th sample is divided into volume elements with the shape of regular rectangular cuboids as in equation (5). For a volume element in the  $n$ th sample, the distances  $t_{0,pqr}^n$  and  $t_{pqr}^n$  inside the sample are calculated as described in Section 2.2. We add the distances traveled inside the other samples in the paths of the incident  $s_0$  and scattered  $s$  beams [Figs. 7 and 5(b)].

The beam paths traveled inside the samples are defined as  $t_{0,pqr}^{m,n}$  and  $t_{pqr}^{m,n}$ , where  $m$  is the sample number outside the corresponding sample  $n$  ( $m \neq n$ ) in the directions of the incident and scattered beam directions  $s_0$  and  $s$ , respectively. To calculate the distances  $t_{0,pqr}^{m,n}$  and  $t_{pqr}^{m,n}$ , we first calculate the distances to the first boundary functions for the  $m$ th sample  $t_n^{s_0}$  and  $t_n^s$  and add a small increment  $\delta$ . Then we define the points  $(x_n^{s_0}, y_n^{s_0}, z_n^{s_0})$  and  $(x_n^s, y_n^s, z_n^s)$  as

**Figure 7**

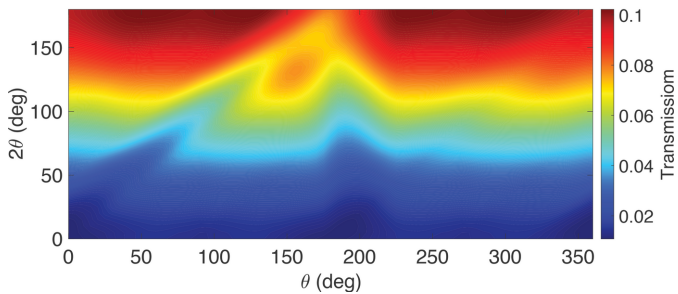
(a) Multiple-sample configuration. In the direction of the  $s_0$  incident beam, we define  $t_{0,pqr}^n$  as the path length from the  $(x_p, y_q, z_r)$  volume element to the boundary function defining the  $n$ th sample,  $t_n^{s_0} + \delta$  as the distance from the volume element to the outside sample  $m$  and  $t_{0,pqr}^{m,n}$  as the total path distance traveled inside the sample  $m$ . In the same way, we define for the  $m+1$  sample the distances  $t_{pqr}^n$ ,  $t_n^s + \delta$  and  $t_{pqr}^{m+1,n}$  in the direction of the  $s$  scattered beam ( $m, m+1 \neq n$ ). (b) For a volume element  $(x_p, y_q, z_r)$  inside the  $n$ th sample, the  $m$ th sample can be located in the way of the incident  $s_0$  and scattered  $s$  beam.

$$\begin{aligned} x_n^{s_0} &= -(t_n^{s_0} + \delta)s_{0x} + x_p, & x_n^s &= (t_n^s + \delta)s_x + x_p, \\ y_n^{s_0} &= -(t_n^{s_0} + \delta)s_{0y} + y_q, & y_n^s &= (t_n^s + \delta)s_y + y_q, \\ z_n^{s_0} &= -(t_n^{s_0} + \delta)s_{0z} + z_r, & z_n^s &= (t_n^s + \delta)s_z + z_r. \end{aligned} \quad (18)$$

We then test whether the points  $(x_n^{s_0}, y_n^{s_0}, z_n^{s_0})$  and  $(x_n^s, y_n^s, z_n^s)$  are located inside the  $m$ th sample. If the points are not located inside the  $m$ th sample, we iterate them to the next boundary of the  $m$ th sample. If the volume elements are located inside the  $m$ th sample, then we calculate the path length  $t_{0,pqr}^{m,n}$  in the  $s_0$  path and  $t_{pqr}^{m,n}$  in the  $s$  path. We repeat this procedure for all the samples and the  $(x_p, y_q, z_r)$  volume elements of all  $N$  samples where  $n \neq m$ . We evaluate the contribution of all the samples in each volume element,

$$\begin{aligned} \langle T \rangle &= \frac{1}{\sum_{n=1}^N \Delta v_n M_n} \\ &\times \sum_{n=1}^N \sum_{pqr}^{V_n} \exp \left\{ - \left[ \mu \left( t_{pqr}^n + \sum_{m \neq n} t_{pqr}^{m,n} \right) \right. \right. \\ &\quad \left. \left. + \mu_0 \left( t_{0,pqr}^n + \sum_{m \neq n} t_{0,pqr}^{m,n} \right) \right] \right\} \Delta v_n, \end{aligned} \quad (19)$$

where  $M$  is the total number of volume elements inside all  $N$  samples. Fig. 8 shows the transmission algorithm of an array of three samples: a cube of  $l = 2$  cm with the center located at  $(2, 2, 2)$ , a sphere with  $r = 1$  cm located at  $(-2, -2, -2)$ , and a cylinder with  $r = 1$  cm and a height of  $l = 1.5$  cm located at  $(-2, 2, 0)$ . The linear absorption correction  $\mu = 2.0 \text{ cm}^{-1}$ . The

**Figure 8**

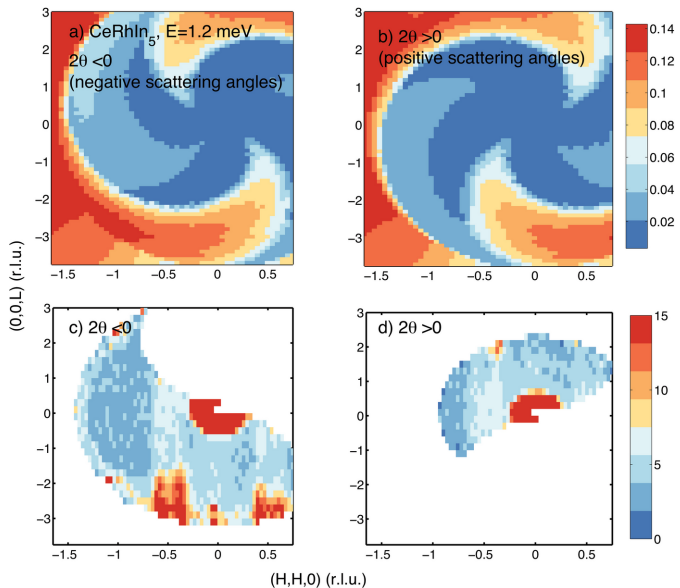
Neutron transmission for three samples: a cube, a sphere and a cylinder. The rotation  $\theta$  and detector position  $2\theta$  are defined as left-handed, which means that positive angles are clockwise, as with most NCNR instruments like the CHRNS-MACS.

incident beam points in the direction of the  $y$  axis and  $s_0 = \hat{y}$  when  $\theta = 0^\circ$ . The sample rotation  $\theta$  is defined as positive when it rotates clockwise, as for the instrument CHRNS-MACS.

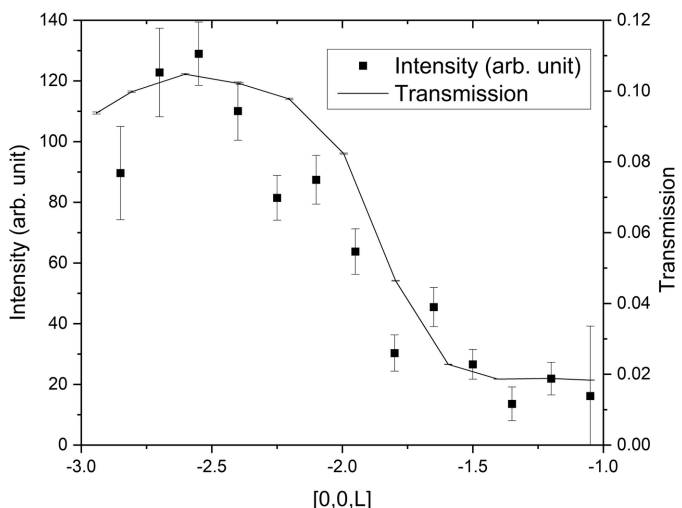
### 3. The case of CeRhIn<sub>5</sub>

CeRhIn<sub>5</sub> is an itinerant antiferromagnet with a tetragonal nuclear structure and a helical magnetic structure (Stock *et al.*, 2015; Dai, 2015; Brener *et al.*, 2024). The compound is structurally related to CeCoIn<sub>5</sub>, which has the highest known heavy fermion superconducting transition temperature ( $T_c = 2.3$  K) (Petrovic *et al.*, 2001), and inelastic scattering measurements have found a strong coupling between magnetic and superconducting fluctuations (Stock *et al.*, 2008; Kenzelmann *et al.*, 2008; Panarin *et al.*, 2009; Blackburn *et al.*, 2010; Kenzelmann *et al.*, 2010; Stock *et al.*, 2012b; Raymond & Lapertot, 2015; Stock *et al.*, 2018). In contrast to CeCoIn<sub>5</sub>, the Rh variant is not a superconductor, except at very low temperatures (Chen *et al.*, 2006; Paglione *et al.*, 2008), well below the onset of spatially long-range antiferromagnetic order (Bao *et al.*, 2000). To formulate a dispersion relation, the MACS spectrometer was used to map out systematically the momentum dependence of the magnetic fluctuations at a series of fixed energy transfers (Rodriguez *et al.*, 2008). The momentum dependence of the magnetic scattering intensity is linked to the direction and correlation of the magnetic moment fluctuations. This quantity is highly angle dependent and therefore it is central to understanding the sample absorption, to understand in turn the underlying physics of this system.

Indium has a large absorption cross section (193.8 barns at a neutron energy of  $E = 25$  meV), and the linear attenuation factor decreases with the incident neutron beam energy from  $\mu = 4.04 \text{ cm}^{-1}$  at  $E = 16$  meV up to  $\mu = 10.36 \text{ cm}^{-1}$  at  $E = 2.4$  meV (Sears, 1992). Rhodium has a similar absorption cross section (144.8 barns at  $E = 25$  meV), making scattering experiments on CeRhIn<sub>5</sub> particularly difficult over other compounds like CeCoIn<sub>5</sub>, for example. The sample was modeled as an irregular slab bounded by an infinite cylinder intersected by five planes:  $x^2 + y^2 - 6.42x + 12.25y = 277.27$ ,  $0.84x + y = 11.62$ ,  $1.13x + y = -15.57$ ,  $0.27x - y = 3.72$ ,  $z = 3.25$  and  $z = -3.25$ . The point that defines the volume of interest is located at the origin. At  $\theta_{\text{sample}} = 2\theta_{\text{sample}} = 0^\circ$ , the incident

**Figure 9**

(a–b) CeRhIn<sub>5</sub> transmission at  $E = 1.2$  meV (Stock *et al.*, 2015; Brener *et al.*, 2024). The total attenuation factor of the sample changes from  $\mu = 7.33 \text{ cm}^{-1}$  at  $E = 5.05$  meV to  $\mu = 5.17 \text{ cm}^{-1}$  at  $E = 9.65$  meV (Sears, 1992). (c–d) In the CeRhIn<sub>5</sub> sample, the mesh scan shows some of the relevant data significantly attenuated at small scattering angles.

**Figure 10**

CeRhIn<sub>5</sub> [00L] neutron line scan at 0.6 meV (left-hand axis) and neutron transmission (right-hand axis). The feature shows a 1D spin interaction in the  $L$  direction. The intensity decay is mainly due to the neutron beam attenuation. Error bars represent one standard deviation.

beam vector  $s_0$  is aligned with the  $z$  axis and the scattering plane lies in the  $zx$  plane. Absorption effects strongly affect the dispersion features, with Figs. 9(a) and 9(b) illustrating the neutron transmission for negative and positive  $2\theta$  angles, respectively. We can observe that the neutron transmission is below 2% due to the long path traveled by the neutrons inside the sample. However, most of the data at high  $2\theta$  values satisfy the scattering reflection geometry of the sample, where the path traveled by the neutrons inside the sample is shorter, giving higher neutron transmission values. The data have a

solid angular dependence, showing the dispersion features of the sample at large  $2\theta$ . Fig. 10 shows how the neutron signal weakens with the neutron transmission of the sample.

#### 4. Program repository

The program repositories and documentation are available in MATLAB and Python at <https://github.com/macsatncnr/abscorrmatlab> and <https://github.com/macsatncnr/abscorppython>.

#### 5. Final remarks

Modern neutron sources and instruments with high neutron flux have made it possible to study highly absorbent samples, particularly in the context of strongly correlated magnetism. Given strong momentum- and hence angle-dependent scattering, careful data analysis must be performed when using this kind of sample due to the features that arise from neutron transmission combined with the sample shape.

The algorithms developed in this paper can be more easily implemented for arbitrary sample geometries than other algorithms and software. For example, the algorithms discussed here can be extended to complex cases like concave surfaces, capillaries and samples that use different bulk materials, simply by re-interpreting the path-length solutions.

#### Acknowledgements

Certain commercial software is identified in this paper to foster understanding. Such identification does not imply recommendation or endorsement by the National Institute of Standards and Technology, nor does it imply that this software is necessarily the best available for the purpose.

#### Funding information

The following funding is acknowledged: National Science Foundation (grant No. DMR-2010792). Access to CHRNS-MACS was provided by the Center for High-Resolution Neutron Scattering, a partnership between the National Institute of Standards and Technology and the National Science Foundation under agreement No. DMR-1508249.

#### References

- Alcock, N. W., Pawley, G. S., Rourke, C. P. & Levine, M. R. (1972). *Acta Cryst.* **A28**, 440–444.
- Angel, R. J. (2004). *J. Appl. Cryst.* **37**, 486–492.
- Arnold, O., Bilheux, J., Borreguero, J., Buts, A., Campbell, S., Chapon, L., Doucet, M., Draper, N., Ferraz Leal, R., Gigg, M., Lynch, V., Markvardsen, A., Mikkelson, D., Mikkelson, R., Miller, R., Palmen, K., Parker, P., Passos, G., Perring, T., Peterson, P., Ren, S., Reuter, M., Savici, A., Taylor, J., Taylor, R., Tolchenov, R., Zhou, W. & Zikovsky, J. (2014). *Nucl. Instrum. Methods Phys. Res. A* **764**, 156–166.
- Bao, W., Pagliuso, P. G., Sarrao, J. L., Thompson, J. D., Fisk, Z., Lynn, J. W. & Erwin, R. W. (2000). *Phys. Rev. B* **62**, R14621–R14624.
- Becker, P. J. & Coppens, P. (1974). *Acta Cryst.* **A30**, 129–147.
- Beer, A. (1852). *Annalen Phys.* **162**, 78–88.
- Blackburn, E., Das, P., Eskildsen, M. R., Forgan, E. M., Laver, M., Niedermayer, C., Petrovic, C. & White, J. S. (2010). *Phys. Rev. Lett.* **105**, 187001.
- Blessing, R. H. (1995). *Acta Cryst.* **A51**, 33–38.
- Bourger, P. (1729). *Essai d'optique sur la gradation de la lumière*. Paris: Claude Jombert.
- Bowden, M. & Ryan, M. (2010). *J. Appl. Cryst.* **43**, 693–698.
- Brener, D. J., Mallo, I. R., Lane, H., Rodriguez-Rivera, J. A., Schmalzl, K., Songvilay, M., Guratinder, K., Petrovic, C. & Stock, C. (2024). *Phys. Rev. B* **110**, 064434.
- Busing, W. R. & Levy, H. A. (1957). *Acta Cryst.* **10**, 180–182.
- Busing, W. R. & Levy, H. A. (1967). *Acta Cryst.* **22**, 457–464.
- Chen, G. F., Matsubayashi, K., Ban, S., Deguchi, K. & Sato, N. K. (2006). *Phys. Rev. Lett.* **97**, 017005.
- Choi, S. K., Coldea, R., Kolmogorov, A. N., Lancaster, T., Mazin, I. I., Blundell, S. J., Radaelli, P. G., Singh, Y., Gegenwart, P., Choi, K. R., Cheong, S.-W., Baker, P. J., Stock, C. & Taylor, J. (2012). *Phys. Rev. Lett.* **108**, 127204.
- Coppens, P. & Hamilton, W. C. (1970). *Acta Cryst.* **A26**, 71–83.
- Cychosz, J. M. & Waggoner, W. N. (1992). *Graphics gems III (IBM version)*, edited by D. Kirk, pp. 275–283. San Francisco: Morgan Kaufmann.
- Dai, P. (2015). *Rev. Mod. Phys.* **87**, 855–896.
- Dallmann, J., Graetz, J. & Hock, R. (2024). *Acta Cryst.* **A80**, 315–328.
- de Meulenaer, J. & Tompa, H. (1965). *Acta Cryst.* **19**, 1014–1018.
- Hermann, H. & Ermrich, M. (1987). *Acta Cryst.* **A43**, 401–405.
- International tables for crystallography* (2006). Vol. C, *Mathematical, physical and chemical tables*, 1st online ed., edited by E. Prince. International Union of Crystallography.
- Kenzelmann, M., Gerber, S., Egetenmeyer, N., Gavilano, J. L., Strässle, T., Bianchi, A. D., Ressouche, E., Movshovich, R., Bauer, E. D., Sarrao, J. L. & Thompson, J. D. (2010). *Phys. Rev. Lett.* **104**, 127001.
- Kenzelmann, M., Strässle, T., Niedermayer, C., Sigrist, M., Padmanabhan, B., Zolliker, M., Bianchi, A. D., Movshovich, R., Bauer, E. D., Sarrao, J. L. & Thompson, J. D. (2008). *Science* **321**, 1652–1654.
- Lu, Y., Duman, R., Beilsten-Edmands, J., Winter, G., Basham, M., Evans, G., Kamps, J. J. A. G., Orville, A. M., Kwong, H.-S., Beis, K., Armour, W. & Wagner, A. (2024). *J. Appl. Cryst.* **57**, 649–658.
- Montesin, T., Jeizmann, J. & Vandon, A. (1991). *Textures Microstruct.* **14–18**, 567–572.
- Paglione, J., Ho, P.-C., Maple, M. B., Tanatar, M. A., Taillefer, L., Lee, Y. & Petrovic, C. (2008). *Phys. Rev. B* **77**, 100505.
- Panarin, J., Raymond, S., Lapertot, G. & Flouquet, J. (2009). *J. Phys. Soc. Jpn* **78**, 113706.
- Pásztorová, J., Howell, A., Songvilay, M., Sarte, P. M., Rodriguez-Rivera, J. A., Arévalo-López, A. M., Schmalzl, K., Schneidewind, A., Dunsiger, S. R., Singh, D. K., Petrovic, C., Hu, R. & Stock, C. (2019). *Phys. Rev. B* **99**, 125144.
- Petrovic, C., Pagliuso, P. G., Hundley, M. F., Movshovich, R., Sarrao, J. L., Thompson, J. D., Fisk, Z. & Monthoux, P. (2001). *J. Phys. Condens. Matter* **13**, L337–L342.
- Pfleiderer, C. (2009). *Rev. Mod. Phys.* **81**, 1551–1624.
- Raymond, S. & Lapertot, G. (2015). *Phys. Rev. Lett.* **115**, 037001.
- Rodriguez, J. A., Adler, D. M., Brand, P. C., Broholm, C., Cook, J. C., Brocker, C., Hammond, R., Huang, Z., Hundertmark, P., Lynn, J. W., Maliszewskyj, N. C., Moyer, J., Orndorff, J., Pierce, D., Pike, T. D., Scharfstein, G., Smee, S. A. & Vilaseca, R. (2008). *Meas. Sci. Technol.* **19**, 034023.
- Rouse, K. D., Cooper, M. J., York, E. J. & Chakera, A. (1970). *Acta Cryst.* **A26**, 682–691.
- Schmitt, D. & Ouladdiaf, B. (1998). *J. Appl. Cryst.* **31**, 620–624.
- Sears, V. F. (1992). *Neutron News* **3**(3), 26–37.
- Shirane, G., Shapiro, S. M. & Tranquada, J. M. (2006). *Neutron scattering with a triple-axis spectrometer: basic techniques*, 1st ed. Cambridge University Press.

- Squires, G. L. (2012). *Introduction to the theory of thermal neutron scattering*, 1st ed. Cambridge University Press.
- Stewart, G. R. (1984). *Rev. Mod. Phys.* **56**, 755–787.
- Stock, C., Broholm, C., Demmel, F., Van Duijn, J., Taylor, J. W., Kang, H. J., Hu, R. & Petrovic, C. (2012a). *Phys. Rev. Lett.* **109**, 127201.
- Stock, C., Broholm, C., Hudis, J., Kang, H. J. & Petrovic, C. (2008). *Phys. Rev. Lett.* **100**, 087001.
- Stock, C., Broholm, C., Zhao, Y., Demmel, F., Kang, H. J., Rule, K. C. & Petrovic, C. (2012b). *Phys. Rev. Lett.* **109**, 167207.
- Stock, C., Rodriguez-Rivera, J. A., Schmalzl, K., Demmel, F., Singh, D. K., Ronning, F., Thompson, J. D. & Bauer, E. D. (2018). *Phys. Rev. Lett.* **121**, 037003.
- Stock, C., Rodriguez-Rivera, J. A., Schmalzl, K., Rodriguez, E. E., Stunault, A. & Petrovic, C. (2015). *Phys. Rev. Lett.* **114**, 247005.
- Thorkildsen, G., Mathiesen, R. H. & Larsen, H. B. (1999). *J. Appl. Cryst.* **32**, 943–950.
- Wuensch, B. & Prewitt, C. (1965). *Z. Kristallogr.* **122**, 24–59.